

Model of spontaneous droplet transport on a soft viscoelastic substrate with nonuniform thickness

S. I. Tamim  and J. B. Bostwick 

Department of Mechanical Engineering, Clemson University, Clemson, South Carolina 29634, USA



(Received 7 May 2021; accepted 13 September 2021; published 24 September 2021)

Dynamic wetting of droplets on soft solids has many industrial and biological applications which require an understanding of the underlying fluid transport mechanism. Here we study the case of a droplet on a viscoelastic substrate of variable thickness which is known to give rise to a spontaneous droplet transport. This phenomenon is known as droplet durotaxis and has been observed experimentally. Here we develop a model assuming a small linear gradient in substrate thickness to reveal the physical mechanism behind this transport phenomena. We show the variable thickness causes an asymmetric deformation along the drop contact line, which causes a variation in the contact angle. This generates a net driving force on the drop, causing it to move in the direction of higher thickness. The resulting drop velocity is determined by balancing the work done by the moving drop with the viscoelastic dissipation of the substrate (viscoelastic braking) and computed from a self-consistent model. We find our results to be in qualitative agreement to previously reported experimental findings.

DOI: [10.1103/PhysRevE.104.034611](https://doi.org/10.1103/PhysRevE.104.034611)

I. INTRODUCTION

Soft surfaces that are easily deformed by capillary forces from a liquid droplet show many unique phenomena during fluid-solid interactions, such as viscosity-independent spreading, stick-slip behavior, and swelling-induced deformation [1–5]. The recent review by Andreotti and Snoeijer [6] provides an overview of the unique physics associated with the various cases of static and dynamic wetting of soft solids as relevant to numerous industrial applications such as controlled droplet manipulation in microfluidics [7], enhanced condensation [8], and evaporation [9]. Spontaneous droplet transport on soft surfaces has received much attention recently, as motivated by the different forms of mechanotaxis found in nature [10–12]. This includes droplet durotaxis, as reported by Style *et al.* [10], in which a drop is spontaneously transported across a soft substrate with gradient in thickness. In this work we study droplet durotaxis by developing a theoretical model to better understand the physics of drop transport in this phenomena.

Droplet durotaxis is inspired by a more general durotaxis phenomenon where living cells tend to move along gradients in the rigidity of their underlying soft substrate [13–15]. Recently, similar behavior have been demonstrated in droplets to create patterns on soft solids [10]. In this experiment, small glycerol drops were placed on a soft silicone substrate with a thickness gradient, and it was found that drops spontaneously moved towards the thicker regions of the substrate. They also noted that the direction of drop motion was opposite to what is observed in living cells. Here we illustrate how elastocapillary deformation can give rise to such motions.

We briefly illustrate the physics of soft wetting. Consider the canonical case of a drop resting on a solid substrate. Here the three-phase contact line of the liquid droplet forms an equilibrium contact angle α with the solid, which is

determined by the classical force balance equation by Young and Dupré [16,17],

$$\gamma_{ls} + \gamma_{lg} \cos \alpha = \gamma_{sg}. \quad (1)$$

Here, γ_{ls} , γ_{lg} , and γ_{sg} are the liquid-solid, liquid-gas, and solid-gas surface tensions, respectively. Note there is a vertical component of γ_{lg} that remains unbalanced and causes the substrate to deform at the contact line. This deformation has size defined by the elastocapillary length scale $\ell_e = \gamma_{lg}/E$, where E is the elastic modulus of the substrate. For wetting by droplets, ℓ_e can be comparable to the size of drop and in this case, the contact line deformation in the solid becomes significant. The substrate is pulled upwards at the contact line, forming a wetting ridge which takes the shape of a triangular cusp [18–20]. The capillary pressure inside the droplet causes the wetting ridge to rotate and change orientation. This rotation also changes the macroscopic contact angle α , which is the angle liquid-gas interface makes with the horizontal line (cf. Fig. 1). As the drop deforms, the equilibrium force balance at the contact line deviates from Young’s law (1) and obeys Neumann’s law for liquid-liquid wetting [21,22] and is given by

$$\vec{\gamma}_{lg} + \vec{\gamma}_{sg} + \vec{\gamma}_{sl} = \vec{0}. \quad (2)$$

For dynamic wetting with a moving contact line, the exact description of force equilibrium can become more complicated [23,24]. This difficulty arises partly due to fact that the solid surface tension is usually not a constant material property but rather a function of the applied strain. This strain dependence is known as the Shuttleworth effect [25] and needs to be considered for cases of large strain in stretched materials [26,27]. In this work we follow Karpitschka *et al.* [28] in assuming a constant solid surface tension and use Neumann’s force balance at the contact line during dynamic

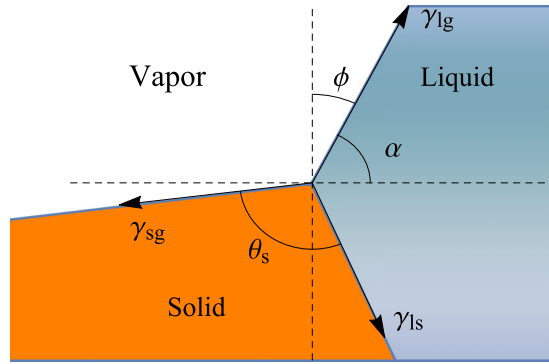


FIG. 1. Orientation of the triangular cusp formed at the tip of the wetting ridge. Macroscopic solid-liquid contact angle α changes as the cusp rotates through a tilt angle ϕ which depends upon the elastic response of the solid substrate. The solid angle formed inside the cusp is denoted as θ_s .

wetting. This is justified given the slow velocities associated with droplet durotaxis and allows us to neglect the Shuttleworth effect. The surface tension of a soft solid is also known to have nontrivial contribution to the deformed shape of its interface [29–31], and we include that effect in our model.

Previous researchers have demonstrated the dependence of the wetting ridge geometry on the substrate thickness, especially for small size droplets [32,33]. As such, one could expect an asymmetric deformation of the wetting ridge, and equivalently, a contact angle asymmetry, for drops on a substrate with thickness gradient. Contact angle asymmetry created by wettability gradients on rigid solids have long been known to generate droplet motion [34–37]. Droplet motion on soft solids have received limited attention so far, in contrast to that on rigid solids. Recently, Bardall *et al.* [38] have studied the possibility of propelling droplets along soft interfaces using either a stiffness gradient or a surface tension gradient. Molecular dynamics studies have also demonstrated the promise of droplet durotaxis by studying the effect of stiffness gradients [39]. Direct numerical simulations have shown the relation between drop velocity and contact angle during motion, proving that contact angle variation drives the drop motion [40].

Drop motion on soft solids such as polymeric gels are known to be strongly dependent on the viscous dissipation within the solid, rather than the liquid [28,41–43]. In our model we assume the substrate to be a linear viscoelastic material with a power-law rheology and compute the response due to the interaction with a liquid drop moving along the free surface with a constant velocity. We assume the liquid viscosity to be small and the drop to retain its spherical cap shape. Here the liquid only interacts with the solid through surface tension forces applied at the contact line and capillary pressure applied along the wet interface.

In this paper we build upon the number of static deformation models that calculate the symmetric deformation profile of the wetting ridge [32,33,44,45] by introducing a variable substrate thickness that results in an asymmetric deformation profile. To simplify our results and focus on the physics of transport, we consider a two-dimensional solid-liquid interface and incorporate a small

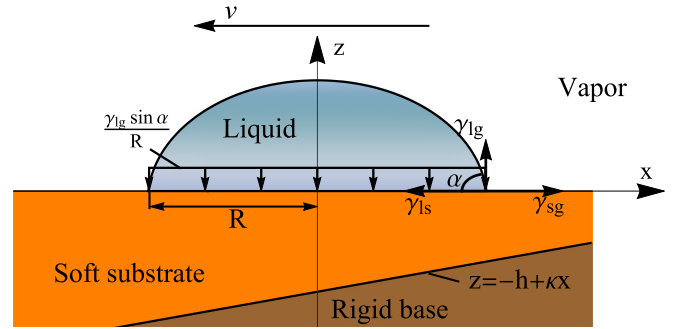


FIG. 2. Definition sketch showing a two-dimensional liquid droplet of radius R in contact with the free surface of a solid substrate with a variable thickness $-h + \kappa x$. The drop applies surface tension forces on the solid at the contact line $x = R$ and bulk fluid pressure along the length of the droplet

unidirectional gradient to the substrate thickness using a boundary perturbation method [46]. This allows us to apply integral transform methods to solve the viscoelastic boundary value problem, in an approach similar to the classic correspondence principle [47]. Our solution delivers the solid deformation profile and advancing/receding macroscopic contact angles, from which we show that the local equilibrium conditions at these two contact points generate a driving force in the direction of the gradient. This driving force is balanced by the viscous dissipation in the solid, giving rise to a steady drop velocity, which we calculate in a self-consistent manner. Our results show reasonable agreement with previously reported experiments. Lastly, we provide some concluding remarks including future directions.

II. FORMULATION OF DYNAMIC WETTING PROBLEM

Consider the two-dimensional geometry shown in Fig. 2 in which a liquid droplet is in contact with the free surface of a soft viscoelastic substrate fixed to a rigid base. The soft substrate has a thickness h at the center of the droplet of radius R . The system shown in Fig. 2 is a moving reference frame with velocity v where the vertical axis always passes through the center of the drop. This is related to a fixed reference frame (x') through the relation $x' = x - vt$. Here we are interested in the case of spontaneous drop motion along the solid interface which arises due to a small thickness gradient κ on the substrate. We consider a linear gradient in thickness from the left to the right side of the droplet, which implies the base of the substrate is located at $z = -h + \kappa x$. Based on experimental observations of such cases we make a number of approximations to simplify the problem. First, the drop is assumed to not deform, i.e., spread, such that the wetted radius R is always maintained. We also limit our analysis to small velocities, which allows us to assume a translational velocity v that is independent of time. In this case the liquid interacts with the solid through surface tension forces only, and the balance of these forces at the contact point creates a local equilibrium contact angle α .

The solid substrate is assumed to be linear viscoelastic with a time-dependent stress-strain relationship given by [48]

$$T_{ij}(t) = 2 \int_{-\infty}^t \mu(t-t') \frac{\partial \varepsilon_{ij}(t')}{\partial t'} dt' + \delta_{ij} \int_{-\infty}^t \lambda(t-t') \frac{\partial \varepsilon_{kk}(t')}{\partial t'} dt', \quad (3)$$

where μ and λ are relaxation moduli related to shear and bulk deformation, respectively. They are related to each other through a constant Poisson's ratio ν as $\lambda = 2\mu\nu/(1-2\nu)$.

The strain field ε_{ij} is related to the two-dimensional displacement field $\mathbf{u} = u_x(x, z)\hat{e}_x + u_z(x, z)\hat{e}_z$ as

$$\varepsilon_{ij} = \frac{1}{2} \left(\frac{\partial u_i}{\partial x_j} + \frac{\partial u_j}{\partial x_i} \right). \quad (4)$$

Since we expect fluid motion to be in the low-Reynolds-number regime, i.e., negligible inertia effects, we can assume a quasi-steady state of motion defined by the equilibrium condition,

$$\nabla \cdot \mathbf{T} = 0. \quad (5)$$

A. Boundary conditions

At the rigid base $z = -h + \kappa x$, a zero displacement condition is enforced,

$$u_x(x, -h + \kappa x, t) = 0, \quad u_z(x, -h + \kappa x, t) = 0. \quad (6)$$

Stress continuity is enforced at the free surface $z = 0$ where the normal stress is balanced by the contributions from Laplace pressure due to curvature of the solid surface and the contact line forces from the droplet,

$$T_{zz}(x, 0, t) = \gamma_s \frac{\partial^2 u_z(x, 0, t)}{\partial x^2} + F_{cl}(x, t). \quad (7)$$

Here we assume a neutrally wetting substrate with the solid surface tension on the dry and wet side being equal, $\gamma_{\text{sg}} \equiv \gamma_s$. In this case a point load directed vertically upwards and a uniformly distributed line load in the opposite direction along the length of the droplet constitute the contact line force being applied by the liquid drop. This combined loading is described as

$$F_{cl}(x, t) = \gamma_{\text{lg}} \left(\delta(R - |x - vt|) - \frac{1}{R} H(R - |x - vt|) \right), \quad (8)$$

where δ and H are the Dirac delta and Heaviside theta functions, respectively. Finally, we consider the solid surface to be free of shear,

$$T_{xz}(x, 0, t) = 0. \quad (9)$$

III. SOLUTION METHOD

A. Frequency domain

The boundary value problem is converted from the time domain to the frequency domain ω by the Fourier

transform [49]

$$\begin{aligned} \tilde{f}(\omega) &= \frac{1}{\sqrt{2\pi}} \int_{-\infty}^{\infty} f(t) e^{-i\omega t} dt, \\ f(t) &= \frac{1}{\sqrt{2\pi}} \int_{-\infty}^{\infty} \tilde{f}(\omega) e^{i\omega t} d\omega. \end{aligned} \quad (10)$$

Applying Eq. (10) to Eq. (3) gives

$$\tilde{T}_{ij}(\omega) = 2\tilde{\mu}(\omega)\tilde{\varepsilon}_{ij}(\omega) + \delta_{ij}\tilde{\lambda}(\omega)\tilde{\varepsilon}_{kk}(\omega). \quad (11)$$

Here $\tilde{\mu}(\omega)$ is defined as [28,42]

$$\tilde{\mu}(\omega) = i\omega \int_0^{\infty} \Psi(t) e^{-i\omega t} dt, \quad (12)$$

where the relaxation function Ψ depends upon the rheology of the viscoelastic material. For crosslinked polymers, such as silicone gels, it follows the power-law relation [28],

$$\Psi(t) = \mu_0 \left[1 + \Gamma(1-n)^{-1} \left(\frac{\tau}{t} \right)^n \right], \quad (13)$$

which yields

$$\tilde{\mu}(\omega) = \mu_0 [1 + (i\omega\tau)^n]. \quad (14)$$

Here μ_0 is the static shear modulus, Γ the gamma function, τ the viscoelastic relaxation timescale, and n the power-law exponent. The classic Kelvin-Voigt model is recovered at $n = 1$. In this work we consider the case where solid viscosity is much larger than the fluid viscosity $\mu_0\tau > \eta_f$, and thus droplet transport is governed primarily by the solid response. Using the stress-strain relation (11) we get the frequency-dependent equilibrium equation

$$(1-2\nu)\nabla^2 \tilde{\mathbf{u}} + \nabla(\nabla \cdot \tilde{\mathbf{u}}) = 0. \quad (15)$$

We express the displacement field $\tilde{\mathbf{u}}(x, z)$ in terms of the Galerkin vector $\tilde{\mathbf{G}}(x, z)$ [50] as

$$\tilde{\mathbf{u}} = 2(1-\nu)\Delta \tilde{\mathbf{G}} - \nabla(\nabla \cdot \tilde{\mathbf{G}}), \quad (16)$$

where $\tilde{\mathbf{G}}(x, z) = \tilde{\zeta}(x, z)\hat{e}_z$. Applying Eq. (16) to the governing equation, Eq. (15), results in a biharmonic equation for the potential function $\tilde{\zeta}(x, z)$,

$$\nabla^4 \tilde{\zeta}(x, z) = 0. \quad (17)$$

B. Boundary perturbation

We assume the thickness gradient κ to be a small parameter and expand the boundary condition (6) at the rigid base to first order of κ ,

$$\tilde{\mathbf{u}}(-h + \kappa x) \approx \tilde{\mathbf{u}}(-h) + \kappa x \frac{\partial \tilde{\mathbf{u}}}{\partial z} \Big|_{z=-h} = 0. \quad (18)$$

Then we consider an asymptotic expansion of the problem in terms of κ ,

$$\tilde{\mathbf{u}} = \tilde{\mathbf{u}}_0 + \kappa \tilde{\mathbf{u}}_1, \quad \tilde{\mathbf{T}} = \tilde{\mathbf{T}}_0 + \kappa \tilde{\mathbf{T}}_1, \quad \tilde{\zeta} = \tilde{\zeta}_0 + \kappa \tilde{\zeta}_1. \quad (19)$$

C. Scaling and nondimensional groups

All lengths are scaled by the droplet radius R and wave numbers by $1/R$ in the problem. Also, time is scaled with the

relaxation timescale τ and frequency by $1/\tau$:

$$x = \bar{x}R, \quad z = \bar{z}R, \quad s = \bar{s}/R, \quad t = \bar{t}\tau, \quad \omega = \bar{\omega}/\tau,$$

$$h_o = \bar{h}_oR, \quad h = \bar{h}R, \quad u = \bar{u}R, \quad v = \frac{\bar{v}R}{\tau}. \quad (20)$$

In the following sections, bars are dropped from the scaled variables for simplicity. This choice of scaling yields the following nondimensional groups:

$$\Gamma_s = \frac{\gamma_s}{\mu_o R} \quad : \text{Solid elastocapillary number}$$

$$\Gamma_l = \frac{\gamma_l}{\mu_o R} \quad : \text{Liquid elastocapillary number}$$

$$\Lambda = \frac{h_o}{R} \quad : \text{Aspect ratio.}$$

D. Zeroth order problem

First we derive the zeroth order base solution which refers to constant thickness, i.e., $\kappa = 0$. The dimensionless boundary value problem at this order is

$$\nabla^4 \tilde{\zeta}_0 = 0, \quad (21a)$$

$$\tilde{T}_{zz0} \Big|_{z=0} = \Gamma_s \frac{\partial^2 \tilde{u}_{z0}}{\partial x^2} \Big|_{z=0} + \Gamma_l \tilde{F}_{cl}, \quad (21b)$$

$$\tilde{T}_{xz0} \Big|_{z=0} = 0, \quad (21c)$$

$$\tilde{u}_{x0} \Big|_{z=-\Lambda} = \tilde{u}_{z0} \Big|_{z=-\Lambda} = 0. \quad (21d)$$

To solve these equations we introduce the spatial Fourier transform pair between horizontal length x and wave number s ,

$$\tilde{f}(s) = \frac{1}{\sqrt{2\pi}} \int_{-\infty}^{\infty} f(x) e^{isx} dx, \quad (22)$$

$$f(x) = \frac{1}{\sqrt{2\pi}} \int_{-\infty}^{\infty} \tilde{f}(s) e^{-isx} ds,$$

which when applied to the biharmonic equation (21a) results in an ordinary differential equation for $\hat{\zeta}_0(s, z, \omega)$,

$$\left(\frac{d^2}{dz^2} - s^2 \right)^2 \hat{\zeta}_0 = 0. \quad (23)$$

E. Zeroth order solution

The general solution of Eq. (23) is given by

$$\hat{\zeta}_0(s, z) = (A + Bs z) \cosh(sz) + (C + Ds z) \sinh(sz), \quad (24)$$

with the constants A, B, C, D to be determined from the boundary conditions in Eqs. (21b)–(21d):

$$[\hat{u}_{x0}(s, -\Lambda), \hat{u}_{z0}(s, -\Lambda)] = 0, \quad (25a)$$

$$\hat{T}_{zz0}(s, 0) + \Gamma_s s^2 \hat{u}_{z0}(s, 0) = \Gamma_l \hat{F}_{cl}(s, \omega), \quad (25b)$$

$$\hat{T}_{xz0}(s, 0) = 0. \quad (25c)$$

Solution of the linear system of equations in Eq. (25) gives the unknowns A, B, C, D . Then the transformed displacement at the free surface $z = 0$ is given by Eq. (16). In what follows we report the solution corresponding to incompressible

materials $\nu = 0.5$, as this represents most soft materials used in experiment. The vertical and horizontal components of the transformed deformation are given by

$$\hat{u}_{z0}(s, z, \omega) = \frac{\Gamma_l \hat{F}_{cl}(s, \omega) N_z(s, z)}{M(s, \omega)}, \quad (26a)$$

$$\hat{u}_{x0}(s, z, \omega) = -i \frac{\Gamma_l \hat{F}_{cl}(s, \omega) N_x(s, z)}{M(s, \omega)}. \quad (26b)$$

The definition of the functions $M(s, \omega)$, $N_z(s, z)$, and $N_x(s, z)$ are given in Appendix A.

The Dirac delta function appearing in Eq. (26) has the following property:

$$\int_{-\infty}^{\infty} f(\omega) \delta(\omega - \omega_0) d\omega = f(\omega_0). \quad (27)$$

This allows us to compute the inverse transform of the deformation field by a single integral such as

$$\mathbf{u}_0(x, z) = \frac{1}{\sqrt{2\pi}} \int_{-\infty}^{\infty} \hat{\mathbf{u}}_0(s, z, -sv) e^{-is(x-vt)} ds. \quad (28)$$

F. First order solution

The dimensionless governing equation and boundary conditions at $O(\kappa)$ are given by

$$\nabla^4 \tilde{\zeta}_1 = 0, \quad (29a)$$

$$\tilde{T}_{zz1} \Big|_{z=0} = \Gamma_s \frac{\partial^2 \tilde{u}_{z1}}{\partial x^2} \Big|_{z=0}, \quad (29b)$$

$$\tilde{T}_{xz1} \Big|_{z=0} = 0, \quad (29c)$$

$$\tilde{u}_{x1} \Big|_{z=-\Lambda} = -x \frac{\partial \tilde{u}_{x0}}{\partial z} \Big|_{z=-\Lambda}, \quad (29d)$$

$$\tilde{u}_{z1} \Big|_{z=-\Lambda} = -x \frac{\partial \tilde{u}_{z0}}{\partial z} \Big|_{z=-\Lambda}. \quad (29e)$$

The functions $\frac{\partial \tilde{u}_{z0}}{\partial z}$ and $\frac{\partial \tilde{u}_{x0}}{\partial z}$ are determined from the zeroth order solution.

We take the general solution of Eq. (29a) to be

$$\tilde{\zeta}_1 = e^{-ix} [(E + Fx) \cosh z + (G + Hx) \sinh z]. \quad (30)$$

The first order deformation components at $z = 0$ in the transformed space are given by

$$\tilde{u}_{z1} = \frac{8e^{ix} x \Lambda \Gamma_l \hat{F}_{cl} \left(-\frac{\omega}{v}, \omega \right) P_z(\omega, z)}{\pi M \left(-\frac{\omega}{v}, \omega \right) Q(\omega, z)}, \quad (31a)$$

$$\tilde{u}_{x1} = \frac{i8e^{ix} x \Lambda \Gamma_l \hat{F}_{cl} \left(-\frac{\omega}{v}, \omega \right) P_x(\omega, z)}{\pi M \left(-\frac{\omega}{v}, \omega \right) Q(\omega, z)}. \quad (31b)$$

Defining $\omega = -sv$, we can compute the first order inverse transformed solutions by the same integral as shown in Eq. (28) and combine with the zeroth order solution to obtain the full deformation field. The functions P_x , P_z , and Q are given in Appendix A.

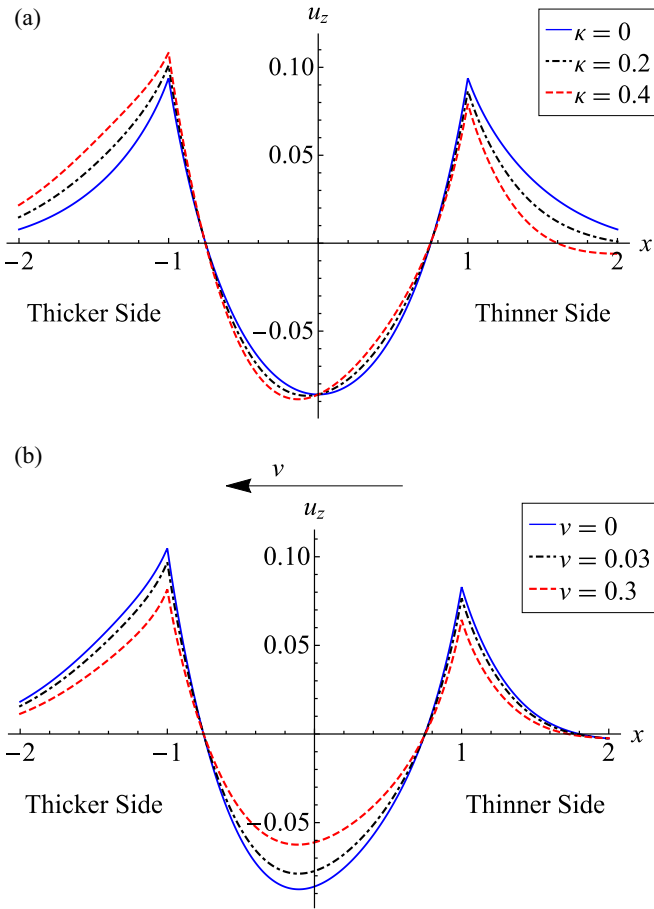


FIG. 3. Vertical deformation u_z of a soft substrate at the liquid-solid interface $z = 0$ as it depends upon (a) thickness gradient κ ($\Lambda = 1$, $\Gamma_s = 1$, $\Gamma_l = 2$, $v = 0$) and (b) dimensionless velocity v ($\Lambda = 1$, $\Gamma_s = 1$, $\Gamma_l = 2$, $\kappa = 0.3$, $n = 0.5$).

IV. RESULTS

A. Deformation of solid substrate

Figure 3 shows the vertical deformation profiles of the solid at the free surface $u_z(x, 0)$ due to a resting liquid droplet. The results are presented here in a moving reference frame putting $x = vt$. Figure 3(a) shows that deformation is symmetric at two sides of the droplet for $\kappa = 0$. For $\kappa > 0$, this symmetry is broken as the liquid drop tends to deform the thicker side of the substrate more than the thinner side. The effect of viscoelasticity on the deformation is illustrated in Fig. 3(b) by plotting $u_z(x, 0)$, as it depends on the dimensionless velocity v . Recall that the viscoelastic timescale is implied within v due to our choice of scaling. We find that increased viscoelastic effects would lead to a decrease in the overall deformation of the solid by the droplet.

The asymmetric deformation caused by the thickness gradient induces a spontaneous motion on the droplet and makes it move towards the direction of higher thickness. This motion is driven by a variation in the macroscopic contact angles α at the two contact points (cf. Fig. 1), which is a result of the asymmetry in deformation at the contact line region. It is known that the solid wetting ridge shown in Fig. 1 assumes a universally triangular shape in the region very close to the

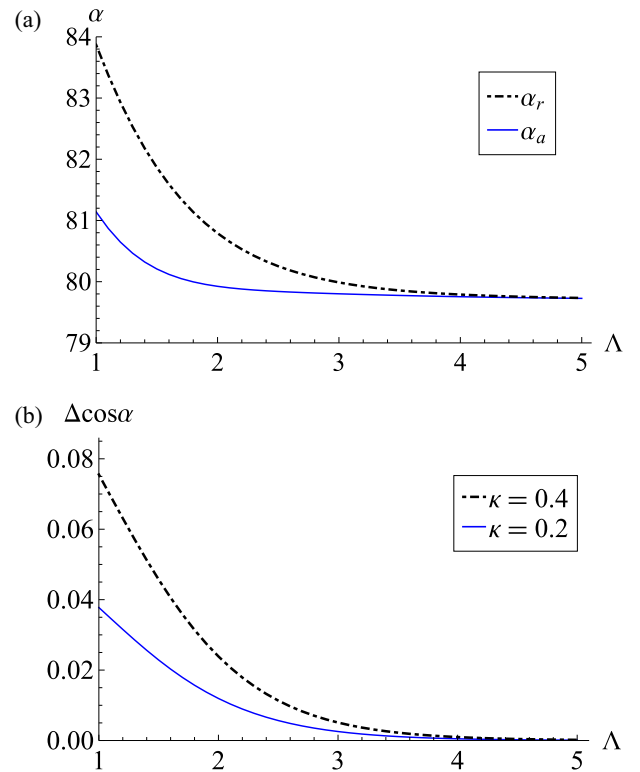


FIG. 4. (a) Advancing (α_a) and receding (α_r) contact angles of the drop in degrees plotted against the aspect ratio Λ . Here $\kappa = 0.25$. (b) Dimensionless driving force $\Delta \cos \alpha$ against Λ for different thickness gradient κ . In both figures, $v = 0$, $\Gamma_s = 0.5$, $\Gamma_l = 2$.

contact line $x \rightarrow 1$ and undergoes a rotation that depends on the aspect ratio of the system [19]. Now, it is possible to obtain the liquid contact angle directly from the rotation ϕ of the wetting ridge given that the surface tension forces maintain a local equilibrium. This equilibrium would hold at the contact line of a moving droplet if the solid angle θ_s , formed within the substrate at the contact line remained constant for different velocities. For a neutrally wetting substrate we have the simple relation $\alpha + \phi = \frac{\pi}{2}$. We can calculate both ϕ and θ_s from the discontinuity of the surface slope $u'_z(x, 0)$ at the contact line, which is given in Appendix B.

We find the cusp rotation angle ϕ to be sensitive to the aspect ratio, which makes the macroscopic contact angle α vary along the contact line, given a thickness gradient exists. We refer to the contact angle on the higher thickness side as the advancing angle α_a and the one on the lower thickness side as the receding angle α_r . In Fig. 4(a) we plot these angles against aspect ratio Λ showing that both of the contact angles decrease as Λ increases, which results from increased rotation of the triangular cusp at the contact line. We note that the difference between the two angles is also inversely related to Λ , and this difference approaches zero for large aspect ratio. As mentioned above, this calculation relies upon the constant θ_s for all v , which we verify in Appendix C.

The difference in contact angles created by the thickness gradient generates an unbalanced horizontal force in the direction of lower contact angle, which drives the droplet. This

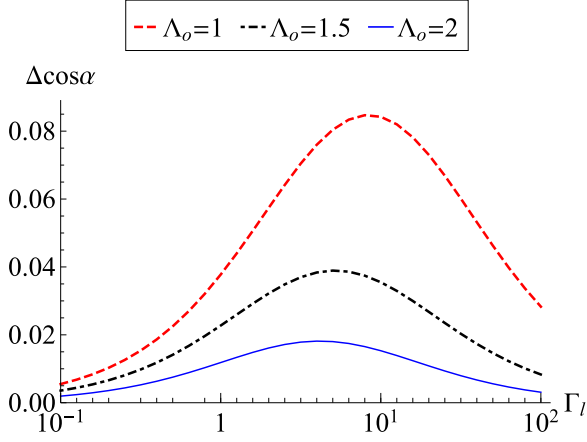


FIG. 5. Driving force $\Delta \cos \alpha$ plotted against the elastocapillary number Γ_l with different aspect ratios Λ . Here, $v = 0.5$, $\Gamma_s = 0.5\Gamma_l$, $\kappa = 0.3$, $v = 0$.

driving force per unit length is

$$F_d = \gamma_g(\cos \alpha_a - \cos \alpha_r). \quad (32)$$

Figure 4(b) plots $\Delta \cos \alpha = \cos \alpha_a - \cos \alpha_r$ against Λ , showing a decreased driving force with increasing substrate thickness. This reduction in the driving force predicts a slowing down of the drop as it moves towards higher thickness regions. Style *et al.* [10] showed similar trends with a non-linear thickness gradient where a decelerating drop eventually comes to rest on a point of high aspect ratio. We note that the presence of surface imperfections will cause contact angle hysteresis, which acts in the opposite direction to the driving force. When the driving force becomes too small to overcome this hysteresis effect, the drop will no longer be able to move. Larger slopes always generate a higher driving force. Similar driving forces have been studied for wetting on rigid solids, where the wettability gradient induces a contact angle asymmetry on liquid drop causing motion [34,35]. The key difference for soft wetting is that a wettability gradient is not essential for generating drop motion. In fact, for the neutral wetting case with $\gamma_{sg} - \gamma_{sl} = 0$ considered in our model here, drop motion is induced through a change in the macroscopic contact angles by the rotation of the wetting ridge.

Figure 5 plots $\Delta \cos \alpha$ against liquid elastocapillary number Γ_l with $\Gamma_s = 0.5\Gamma_l$. Here we find that $\Delta \cos \alpha$ increases with increasing elastocapillarity until it reaches a maximum value beyond which it starts to decrease. The maximum driving force is found to occur at around $\Gamma \sim 1$. A lower elastocapillary effect is typically associated with small solid deformation, resulting in a trivial amount of rotation of the wetting ridge. On the other hand, a high elastocapillary effect means the capillary pressure, which scales as $O(\Gamma_l)$ and pushes the solid downward, becomes large. In this case the substrate essentially behaves like a fluid, making the effect of underlying thickness negligible.

The driving force on a droplet also depends on the velocity due to the viscoelastic response of the substrate. Figure 6 plots $\Delta \cos \alpha$ against the scaled velocity v , as it depends upon the power-law exponent n . From (14) we know that increasing n increases both the storage (μ') and loss modulus (μ''), which

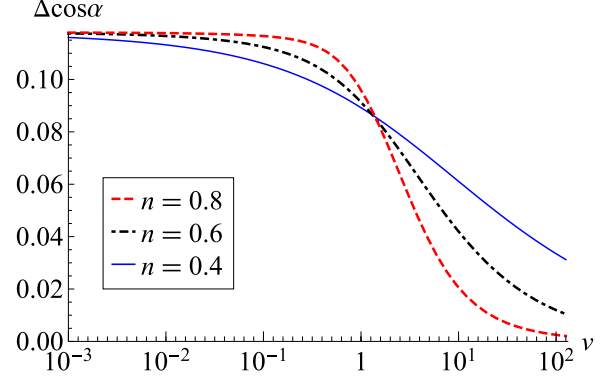


FIG. 6. Driving force $\Delta \cos \alpha$ against scaled velocity v for different power-law exponent n . Here, $\Lambda = 1$, $\Gamma_s = 2$, $\Gamma_l = 5$, $\kappa = 0.4$.

are given by

$$\mu' = \mu_0 \left[1 + (\omega\tau)^n \cos \frac{n\pi}{2} \right], \quad \mu'' = \mu_0 (\omega\tau)^n \sin \frac{n\pi}{2}. \quad (33)$$

We find that $\Delta \cos \alpha$ decreases with increasing velocity. The effect of n is observed in two different regions with a transition point at $v \sim 1$. For $v < 1$ we find a higher driving force at the same velocity for higher n . This is the region where μ' is higher than μ'' . For $v > 1$, driving force decreases with increasing n , where μ'' becomes larger than μ' .

B. Velocity of the moving drop

Our deformation model predicts the driving force exerted on the drop. For gradient-driven droplet motion on rigid substrates, a steady state velocity is obtained from a steady state force balance between the driving force and the resistive viscous force,

$$P_f + P_s = F_d v. \quad (34)$$

Here P_f and P_s are the dissipated powers within the fluid and solid, respectively. The dissipation in the fluid scales with fluid viscosity η_f and can be analytically determined assuming slow Poiseuille flow as [51]

$$P_f \cong \frac{3\eta_f v^2}{\alpha} \ln r_c. \quad (35)$$

Here r_c is a ratio of cutoff length scales to remove the contact line singularity. The typical value of $\ln r_c$ is $O(10)$. For motion on a rigid substrate, the dissipation occurs primarily in the fluid and one need not consider P_s in Eq. (34). However, the opposite is true for most soft substrates. Viscoelasticity in a soft solid can significantly affect the liquid motion, reducing its velocity by orders of magnitude in a phenomenon known as viscoelastic braking [2]. Therefore to accurately predict drop velocity on a soft substrate, we need to calculate the dissipation within the solid,

$$P_s = \int T_{ij} : \frac{\partial \varepsilon_{ij}}{\partial t} d^2x, \quad (36)$$

which can be expressed as an integral over the free surface using the divergence theorem,

$$P_s = \oint \vec{T} \cdot \frac{\partial \vec{u}}{\partial t} ds. \quad (37)$$

This approach was followed by Van Gorcum *et al.* [23] and allows further simplification for incompressible materials which only have a single nonzero stress component at the free surface $z = 0$. If we consider the free surface to extend over an infinite domain in the horizontal extent, then Eq. (37) becomes

$$P_s = \int_{-\infty}^{\infty} T_{zz}(x, 0, t) \frac{\partial u_z}{\partial t}(x, 0, t) dx. \quad (38)$$

Writing this integral in terms of the spatial transform, we get

$$P_s = \frac{\mu_0 R^2}{\tau} \int_{-\infty}^{\infty} dx \int_{-\infty}^{\infty} ds \hat{T}_{zz}(s, 0) e^{-is(x-vt)} \times \int_{-\infty}^{\infty} ds' (is'v) \hat{u}_z(s', 0) e^{-is'(x-vt)}. \quad (39)$$

The case of an infinitely wide solid substrate only applies to the $\kappa = 0$ case. Therefore in order to make progress we use the zeroth order solutions to evaluate the integral in Eq. (39). Since we consider κ to be a small parameter, the zeroth order analysis should provide us with an estimate for the scale of the dissipated power. Keeping the real part of the dissipated power only we can write

$$P_s \cong \frac{1}{\tau} \mu_0 R^2 v^{n+1} \Gamma_l^2 H, \quad (40)$$

with

$$H = \int_{-\infty}^{\infty} ds \frac{2s^{n+2} (\hat{F}_{cl}(s))^2}{[M(s, -sv)]^2} [2s\Lambda - \sinh(2s\Lambda)] \times [1 + 2s^2\Lambda^2 + \cosh(2s\Lambda)]. \quad (41)$$

For low velocities we can approximate, $M(s, -sv) \approx M(s, 0)$, to simplify the computation. Putting Eqs. (35) and (40) in the force balance (34) we get the following dimensionless equation:

$$v^n \Gamma_l^2 H + \frac{3\epsilon}{\alpha} \ln r_c \cong \Gamma_l \Delta \cos \alpha. \quad (42)$$

Here $\epsilon = \eta/\mu_0\tau$ is a viscosity ratio, typically a small parameter in viscoelastic wetting experiments, especially when the viscoelastic timescale $\tau \approx 0.1$ – 1 s. Therefore in this work we limit our analysis to the $\epsilon \rightarrow 0$ case and assume that solid viscosity gives the dominant dissipation in the force balance (42), which gives the following equation for velocity:

$$v \cong \left(\frac{\Delta \cos \alpha}{\Gamma_l H} \right)^{1/n}. \quad (43)$$

We combine Eq. (43) with the solution for $\Delta \cos \alpha$ derived in the previous sections and determine the magnitude of the velocity of a spontaneously moving drop on a soft substrate. We do this in a self-consistent manner where we calculate the driving force for a initial velocity guess, fit the solution to Eq. (43), and iteratively find the correct velocity that satisfies this equation.

Previously, Long *et al.* [42] derived an expression for the solid dissipation with similar rheology. They assumed a small elastocapillary effect and calculated dissipation over a small domain of wave numbers where substrate thickness has negligible influence on the dynamics. In contrast, droplet durotaxis typically involves finite elastocapillarity and substrate thickness, which can have a significant effect on the

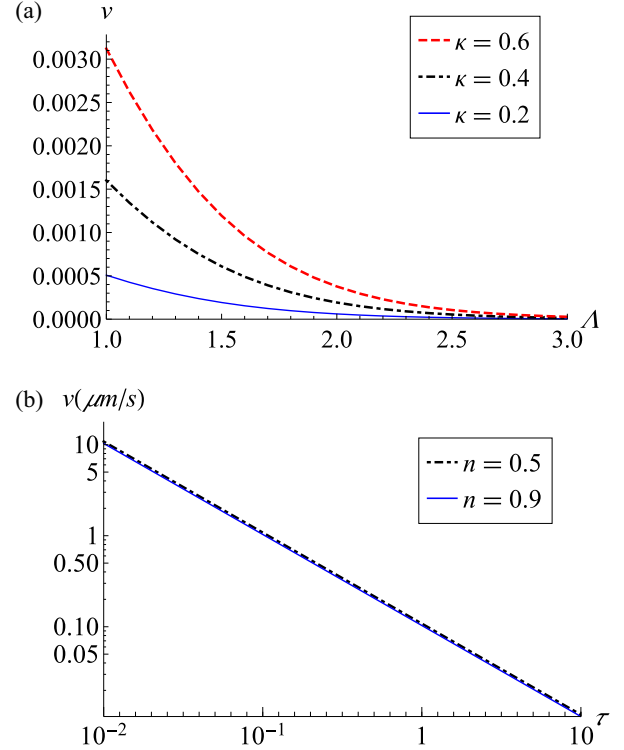


FIG. 7. (a) Dimensionless velocity v plotted against aspect ratio Λ with different thickness gradient κ . Here, $\Gamma_s = 1$, $\Gamma_l = 2$, $n = 0.6$. (b) Velocity in $\mu\text{m/s}$ plotted against relaxation timescale τ with different power-law exponent n . Here, $\Lambda = 1$, $\Gamma_s = 3$, $\Gamma_l = 6$, $\kappa = 0.4$, $R = 10 \mu\text{m}$.

solid dissipation. These are incorporated in our current numerical solution and provide a more reliable method to calculate the drop velocity.

Figure 7(a) plots the scaled velocities v obtained using this method against aspect ratio Λ . We see that drop velocity reduces with increasing Λ , similar to $\Delta \cos \alpha$ in Fig. 4(b). We also find higher velocities for higher values of κ as expected. Figure 7(b) shows the dependence of drop velocity on the viscoelastic parameters τ and n . Higher τ reflects a longer relaxation time in the solid and therefore a smaller predicted velocity. The power-law exponent n has little effect on the velocity.

Style *et al.* [10] observed the motion of microsized glycerol droplets on a PDMS substrate with a nonlinear thickness gradient. They reported velocities as high as $v \sim 0.1 \mu\text{m/s}$ in the shallowest regions of the substrate. We find from Eq. (43) that the drop velocity is strongly dependent on the elastocapillary numbers, as well as the viscoelastic parameters. Therefore one needs to know the exact value of the material parameters to accurately compare the experimental findings with the theoretical prediction. For example, we consider $R = 7 \mu\text{m}$, $\Lambda = 0.8$, and $\kappa = 0.4$ to represent one droplet reported in the experiment which had $v \approx 0.08 \mu\text{m/s}$. If we let $\mu_0 = 1 \text{ kPa}$, $\gamma_s = 0.04 \text{ N/m}$, $\gamma_l = 0.06 \text{ N/m}$, $n = 0.8$, $\tau = 0.5 \text{ s}$, our model predicts a drop velocity of $0.2 \mu\text{m/s}$, which is close to the experimental value. The slightly higher numerical value of theoretical prediction could be due to the

contact angle hysteresis, which would tend to decrease the drop velocity.

V. CONCLUSION

We have developed a two-dimensional boundary perturbation model for the deformation of a soft viscoelastic substrate due to a rigid droplet moving along the interface with velocity v across its interface. The competition between elasticity and capillary forces is characterized by nondimensional elastocapillary numbers for the solid and liquid, while viscoelasticity is described using a power-law model for the complex shear modulus. A small linear gradient in the substrate thickness is shown to change the contact angle along the contact line and generate a net driving force in the direction of increasing substrate thickness. We compute the contact angles by measuring the rotation of the triangular cusp at the tip of the wetting ridge. Here, Neumann's law requires the solid angle to remain constant for a moving drop, and we show that this is valid for droplets moving at low velocities. The drop velocity is determined using a self-consistent calculation balancing the power with viscous dissipation in the solid. We show the drop velocity decreases with increasing aspect ratio, in agreement with experiments on droplet durotaxis. We also show the sensitivity of the drop velocity on the viscoelastic parameters in the solid, where increased relaxation time of the solid reduces the velocity. Our predictions compare favorably to the experiments of Style *et al.* [10] when using reasonable parameter values.

We have identified the parameter regimes more favorable to droplet motion, and those should provide directions for designing future experiments and shed light on the droplet durotaxis phenomena. Cell motility in nature by durotaxis is typically attributed to the inherent ability of the cells to probe the elasticity of the substrate by exerting traction forces. The elastocapillary mechanism offers an alternative and simpler understanding of this biological process from a transport perspective. More experimental investigation is needed to determine under what circumstances the cell motion becomes independent of the internal properties of the cell and follows the simple drop transport mechanism described here. While cells move from lower to higher stiffness regions, droplet motion occurs in the opposite direction. This discrepancy has been attributed to the wetting conditions of the solid in literature [52]. Incorporating partial wetting effects is a natural extension to our model and needs to be investigated in future works to compare with cellular durotaxis.

Our droplet transport model could be verified by analyzing thickness gradients seen in experiment. For example, the experiments of Style *et al.* [10] investigated drop motion on a nonlinear thickness gradient. Solving this problem with nonlinear gradients could shed light on the effect that different types of gradients might have on the droplet transport. In our model we have assumed a nontrivial but constant capillary pressure from the liquid drop on a solid substrate, which is important for small droplets and had not been included in previous dynamic wetting models. If the contact angle difference is large, the free surface of the drop will be significantly deformed and our analysis would need to be modified. Future works could focus on developing new techniques to

include these effects in the dynamic model. Finally, we have ignored the effect of liquid viscosity, which affects the dynamic contact angle for rigid substrates [53,54]. The cases where solid and liquid viscosity are of the same scale have only received limited attention so far [24,55]. A more general model is desired to reinterpret classical wetting models for rigid substrates to soft surfaces which would enable us to exploit the unique properties of soft wetting in many industrial applications.

ACKNOWLEDGMENT

J.B.B. acknowledges support from NSF Grant No. CBET-1750208.

APPENDIX A: FUNCTIONS DEFINED IN THE SOLUTION OF DEFORMATION

The functions defined in Eq. (26) are given by

$$M(s, \omega) = s[2(1 + (i\omega\tau)^n)(1 + 2s^2\Lambda^2 + \cosh(2s\Lambda)) + s\Gamma_s(\sinh(2s\Lambda) - 2s\Lambda)],$$

$$N_z(s, z) = [1 + 2s^2\Lambda(z + \Lambda)\sinh(sz) + \sinh(s(z + 2\Lambda))] - s(z + 2\Lambda)\cosh(sz) - sz\cosh(s(z + 2\Lambda)),$$

$$N_x(s, z) = 2s\Lambda(z + \Lambda)\cosh(sz) - z[\sinh(sz) + \sinh(s(z + 2\Lambda))].$$

The functions in Eq. (29) are given by

$$P_z(\omega, z) = \cosh z\{2(1 + (i\omega)^n)(z + \Lambda)\cosh \Lambda + z[\Gamma_s - 2\Lambda(1 + (i\omega)^n)]\sinh \Lambda\} - \Lambda[\Gamma_s + 2z(1 + (i\omega)^n)]\sinh z\cosh \Lambda,$$

$$P_x(\omega, z) = \sinh \Lambda(\cosh z + z\sinh z)[2\Lambda(1 + (i\omega)^n) - \Gamma_s] \times [2(z\Lambda - 1)(1 + (i\omega)^n) + \Lambda\Gamma_s]\cosh z\cosh \Lambda - 2z(1 + (i\omega)^n)\sinh z\cosh \Lambda,$$

$$Q(\omega, z) = 2(1 + (i\omega)^n)(1 + 2\Lambda^2 + \cosh(2\Lambda)) + \Gamma_s(\sinh(2\Lambda) - 2\Lambda).$$

The contact line force is

$$\hat{F}_{cl}(s, \omega) = \sqrt{\frac{2}{\pi}} \left(\cos s - \frac{\sin s}{s} \right) \delta(\omega + sv). \quad (\text{A1})$$

APPENDIX B: DETERMINING CUSP ROTATION AND SOLID ANGLE

The cusp rotation ϕ and the solid angle θ_s are calculated from the following relations using the slope at the contact point $u'_z(x, 0)$:

$$\phi = \frac{1}{2}(\tan^{-1} \lim_{x \rightarrow 1_+} u'_z(x, 0) - \tan^{-1} \lim_{x \rightarrow 1_-} u'_z(x, 0)), \quad (\text{B1a})$$

$$\theta_s = 180 - (\tan^{-1} \lim_{x \rightarrow 1_+} u'_z(x, 0) + \tan^{-1} \lim_{x \rightarrow 1_-} u'_z(x, 0)). \quad (\text{B1b})$$

The + and - signs refer to the wet and dry sides of solid, respectively. Here we obtain the slope $u'_z(x, 0)$ using the

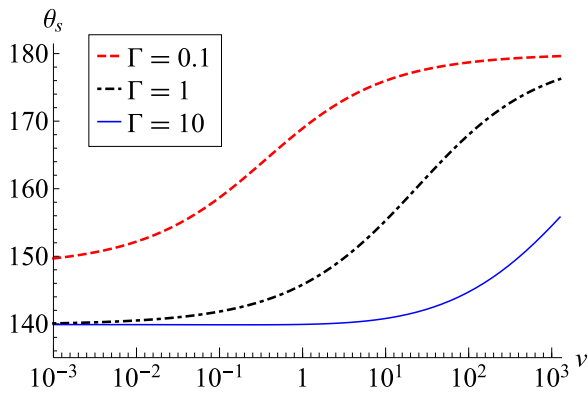


FIG. 8. Solid angle θ_s plotted against the scaled velocity v with different elastocapillary numbers Γ_s . Here, $\Lambda = 1$, $\Gamma_s = 0.5\Gamma_l$, $n = 0.5$, $\kappa = 0.3$.

following property of the Fourier transform:

$$\int_{-\infty}^{\infty} \frac{df(x)}{dx} e^{isx} dx = -is \int_{-\infty}^{\infty} f(x) e^{isx} dx. \quad (\text{B2})$$

APPENDIX C: VALIDITY OF THE NEUMANN FORCE BALANCE IN DYNAMIC WETTING

Figure 8 plots the cusp angle θ_s against dimensionless velocity v for different elastocapillary numbers. This shows that for small values of Γ_s , which refers to either a nearly rigid substrate or a large droplet, θ_s increases with increasing velocity until it reaches the maximum value of 180° . This means that Neumann's equilibrium does not hold for this case. As we increase Γ_s , θ_s tends to remain constant over a wider range of velocity before starting to increase. Therefore Neumann's equilibrium is sufficient for predicting the contact angle for this velocity range. Since the droplet durotaxis phenomenon has been found to occur at low velocity with elastocapillary numbers $\Gamma \sim O(1)$, we proceed with the assumption of Neumann's triangular force equilibrium at the contact line is valid for our analysis. We also find the solid angle θ_s to be independent of the substrate thickness, in line with previous findings [56].

- [1] M. Shanahan, *J. Phys. D* **20**, 945 (1987).
- [2] M. Shanahan and A. Carre, *Langmuir* **11**, 1396 (1995).
- [3] T. Kajiyama, A. Daerr, T. Narita, L. Royon, F. Lequeux, and L. Limat, *Soft Matter* **9**, 454 (2013).
- [4] M. van Gorcum, B. Andreotti, J. H. Snoeijer, and S. Karpitschka, *Phys. Rev. Lett.* **121**, 208003 (2018).
- [5] A. Pandey and D. P. Holmes, *Soft Matter* **9**, 5524 (2013).
- [6] B. Andreotti and J. H. Snoeijer, *Annu. Rev. Fluid Mech.* **52**, 285 (2020).
- [7] A. A. Darhuber and S. M. Troian, *Annu. Rev. Fluid Mech.* **37**, 425 (2005).
- [8] M. Sokuler, G. K. Auernhammer, M. Roth, C. Liu, E. Bonaccorso, and H.-J. Butt, *Langmuir* **26**, 1544 (2009).
- [9] M. C. Lopes and E. Bonaccorso, *Soft Matter* **8**, 7875 (2012).
- [10] R. W. Style, Y. Che, S. J. Park, B. M. Weon, J. H. Je, C. Hyland, G. K. German, M. P. Power, L. A. Wilen, J. S. Wettlaufer *et al.*, *Proc. Natl. Acad. Sci. USA* **110**, 12541 (2013).
- [11] J. Bueno, Y. Bazilevs, R. Juanes, and H. Gomez, *Extreme Mech. Lett.* **13**, 10 (2017).
- [12] A. T. Bradley, F. Box, I. J. Hewitt, and D. Vella, *Phys. Rev. Lett.* **122**, 074503 (2019).
- [13] C.-M. Lo, H.-B. Wang, M. Dembo, and Y.-I. Wang, *Biophys. J.* **79**, 144 (2000).
- [14] D. E. Discher, P. Janmey, and Y.-I. Wang, *Science* **310**, 1139 (2005).
- [15] L. Trichet, J. Le Digabel, R. J. Hawkins, S. R. K. Vedula, M. Gupta, C. Ribault, P. Hersen, R. Voituriez, and B. Ladoux, *Proc. Natl. Acad. Sci.* **109**, 6933 (2012).
- [16] T. Young, *Philos. Trans. Royal Soc. Lond.* **95**, 65 (1805).
- [17] A. Dupré and P. Dupré, *Théorie mécanique de la chaleur* (Gauthier-Villars, 1869).
- [18] G. Lester, *J. Colloid Sci.* **16**, 315 (1961).
- [19] R. W. Style, R. Boltyanskiy, Y. Che, J. S. Wettlaufer, L. A. Wilen, and E. R. Dufresne, *Phys. Rev. Lett.* **110**, 066103 (2013).
- [20] S. J. Park, B. M. Weon, J. San Lee, J. Lee, J. Kim, and J. H. Je, *Nat. Commun.* **5**, 4369 (2014).
- [21] F. E. Neumann, *Vorlesungen über die Theorie der Capillarität* (B.G. Teubner, Leipzig, 1894).
- [22] A. Marchand, S. Das, J. H. Snoeijer, and B. Andreotti, *Phys. Rev. Lett.* **109**, 236101 (2012).
- [23] M. Van Gorcum, S. Karpitschka, B. Andreotti, and J. Snoeijer, *Soft Matter* **16**, 1306 (2020).
- [24] J. Dervaux, M. Roche, and L. Limat, *Soft Matter* **16**, 5157 (2020).
- [25] R. Shuttleworth, *Proc. Phys. Soc., Sect. A* **63**, 444 (1950).
- [26] Q. Xu, R. W. Style, and E. R. Dufresne, *Soft Matter* **14**, 916 (2018).
- [27] J. H. Snoeijer, E. Rolley, and B. Andreotti, *Phys. Rev. Lett.* **121**, 068003 (2018).
- [28] S. Karpitschka, S. Das, M. van Gorcum, H. Perrin, B. Andreotti, and J. H. Snoeijer, *Nat. Commun.* **6**, 7891 (2015).
- [29] S. Tamim and J. Bostwick, *Soft Matter* **15**, 9244 (2019).
- [30] S. Tamim and J. Bostwick, *Soft Matter* **17**, 4170 (2021).
- [31] S. Mora, T. Phou, J.-M. Fromental, L. M. Pismen, and Y. Pomeau, *Phys. Rev. Lett.* **105**, 214301 (2010).
- [32] R. W. Style and E. R. Dufresne, *Soft Matter* **8**, 7177 (2012).
- [33] J. B. Bostwick, M. Shearer, and K. E. Daniels, *Soft Matter* **10**, 7361 (2014).
- [34] F. Brochard, *Langmuir* **5**, 432 (1989).
- [35] R. S. Subramanian, N. Moumen, and J. B. McLaughlin, *Langmuir* **21**, 11844 (2005).
- [36] S. Daniel and M. K. Chaudhury, *Langmuir* **18**, 3404 (2002).
- [37] M. K. Chaudhury and G. M. Whitesides, *Science* **256**, 1539 (1992).
- [38] A. Bardall, S.-Y. Chen, K. E. Daniels, and M. Shearer, *IMA J. Appl. Math.* **85**, 495 (2020).
- [39] P. E. Theodorakis, S. A. Egorov, and A. Milchev, *J. Chem. Phys.* **146**, 244705 (2017).
- [40] H. Gomez and M. Velay-Lizancos, *Eur. Phys. J. Special Topics* **229**, 265 (2020).

- [41] A. Carre and M. E. Shanahan, *Langmuir* **11**, 24 (1995).
- [42] D. Long, A. Ajdari, and L. Leibler, *Langmuir* **12**, 5221 (1996).
- [43] S. Park, J. Bostwick, V. De Andrade, and J. Je, *Soft Matter* **13**, 8331 (2017).
- [44] E. R. Jerison, Y. Xu, L. A. Wilen, and E. R. Dufresne, *Phys. Rev. Lett.* **106**, 186103 (2011).
- [45] A. Bardall, K. E. Daniels, and M. Shearer, *Eur. J. Appl. Math.* **29**, 281 (2018).
- [46] I. Herrera, *J. Geophys. Res.* **69**, 3845 (1964).
- [47] G. Graham, *Q. Appl. Math.* **26**, 167 (1968).
- [48] R. Christensen, *Theory of Viscoelasticity: An Introduction* (Elsevier, New York, 2012).
- [49] I. N. Sneddon, *Fourier Transforms* (McGraw-Hill Book Company, New York, 1951).
- [50] R. W. Soutas-Little, *Elasticity* (Courier Corporation, North Chelmsford, MA, 1999).
- [51] P.-G. De Gennes, *Rev. Mod. Phys.* **57**, 827 (1985).
- [52] J. Bueno, Y. Bazilevs, R. Juanes, and H. Gomez, *Soft Matter* **14**, 1417 (2018).
- [53] R. Cox, *J. Fluid Mech.* **168**, 169 (1986).
- [54] O. Voinov, *Fluid Dyn.* **11**, 714 (1976).
- [55] V. Charitatos and S. Kumar, *Soft Matter* **16**, 8284 (2020).
- [56] L. Limat, *Eur. Phys. J. E* **35**, 134 (2012).